Experiments in Fluids (2006) 40: 80–97
DOI 10.1007/s00348-005-0048-y

RESEARCH ARTICLE

T. Corpetti · D. Heitz · G. Arroyo · E. Mémin
A. Santa-Cruz

Fluid experimental flow estimation based on an optical-flow scheme

Received: 30 January 2005 / Revised: 30 May 2005 / Accepted: 29 July 2005 / Published online: 18 October 2005

Abstract We present in this paper a novel approach dedicated to the measurement of velocity in fluid experimental flows through image sequences. Unlike most of the methods based on particle image velocimetry (PIV) approaches used in that context, the proposed technique is an extension of "optical-flow" schemes used in the computer vision community, which includes a specific enhancement for fluid mechanics applications. The method we propose enables to provide accurate *dense* motion fields. It includes an image based integrated version of the continuity equation. This model is associated to a regularization functional, which preserve divergence and vorticity blobs of the motion field. The method was applied on synthetic images and on real experiments carried out to allow a thorough comparison with a state-of-the-art PIV method in conditions of strong local free shear.

Keywords Fluid motion measurement · Continuity equation · Div–curl regularization · Optical-flow · PIV

1 Introduction

In the experimental fluid mechanics domain, imaging techniques now routinely produce various types of videos which constitute a unique source of information for both applied and theoretical studies (Adrian 1991; Wallace and Foss 1995; Wernert et al. 1996). In such a context, cameras provide in a versatile and non-intrusive way huge amounts of (almost) continuous spatio-temporal data, as opposed to in situ measurement techniques (e.g., thermal anemometry), which supply only sparse spatial information. On the other hand, unlike dedicated probes, images only give indirect access to the physical quantities of interest. With videos or image series, one must face the complex task of extracting these quantities from the intensity patterns recorded in the successive images. As compared to more classical motion analysis problems addressed by the computer vision community, the analysis of fluid motion from images is particularly challenging due to the great deal of spatial and temporal distortions that the intensity patterns exhibit.

In most of the domains requiring experimental fluid flow visualization and measurement, particle image velocimetry (PIV) techniques or related methods play an important role and are intensively used to provide motion estimation. These techniques are based on a spatio-temporal cross-correlation submitted to a consistency assumption of the flow within a local interrogation window. The interrogation windows generally contain several particles with different motions. Considering a unique motion vector for all these particles may lead in some circumstances to a very poor local motion representation.

In the computer vision community, obtaining the "optical flow" consists in extracting a *dense* representation of the motion field (i.e. one vector per pixel). Most of these methods are based on a formulation introduced by Horn and Schunck (1981) in the early 80s, and consist in estimating a vectorial function by minimizing an objective functional. This functional is composed of two terms; the data model and a regularization term. The former is an adequacy term between the unknown motion function and the data. It generally relies on a brightness consistency assumption. Similarly to correlation techniques, this assumption states that a given point keeps its intensity along its trajectory. The latter promotes a global smoothness of the motion field over the image. It must be pointed out that these techniques have been devised for the analysis of quasi-rigid motions with stable salient features. Unfortunately, there is no such thing as an

T. Corpetti (✉) · D. Heitz · G. Arroyo · A. Santa-Cruz
Cemagref 17, avenue de Cucillé,
35044 Rennes Cedex, France
E-mail: thomas.corpetti@uhb.fr

E. Mémin
IRISA/INRIA Campus, Universitaire de Beaulieu,
35042 Rennes Cedex, France

Present address: T. Corpetti
Laboratoire COSTEL UMR 6554 LETG, Maison de la Recherche,
Place du Recteur Henri Le Moal,
35043 Rennes Cedex, France

"object" in most imaged fluid flows which contain mainly deformable and transient brightness patterns. On these sequences, techniques based on standard computer vision ingredients are thus intrinsically limited. The design of alternative approaches dedicated to fluid motion thus remains a widely open research domain.

In this paper, we propose an optical-flow method which permits to extract reliable dense motion fields. This method is dedicated to the analysis of image sequences of fluid flows. It includes, in the data-model term and in the smoothness term, specific adaptations consistent with the physics of flow motion.

This article is organized as follows. In the first section, we present the conventional approaches frequently used by the fluid mechanics community to extract velocity measurements from PIV images. Then, in the second section, we present the proposed alternative. In the last section, results from synthetic images and experiments on two classical flows, a mixing layer and the near wake of a circular cylinder, are presented and analysed. We provide some elements of comparison of our method with a state-of-the-art commercial PIV system.

2 PIV approaches

2.1 Overview

Particle image velocimetry methods are mainly used in fluid mechanics for their known advantages (non-intrusive sensor, ability to obtain relevant instantaneous velocity fields,...). The idea is to visualize, through a laser sheet pulse associated to a camera, a plane area of the flow sowed with luminescent/illuminated particles. A temporal correlation analysis of the images provides motion measurements of the observed particles. Unlike dedicated probes which are able to obtain directly the desired measurements, the velocity is here extracted from the brightness information of the image sequence.

Since the 70s, numerous methods have been proposed to extract velocity fields from particle images. See for instance (Adrian 1991; Raffel et al. 2000) for an extended bibliography on the subject. In the next sections, we will further describe common PIV approaches.

2.2 Computation of the motion field in PIV systems

Most of the PIV systems rely on correlation functions such as "auto-correlation" (if only one image containing the traces of particles is available) or "cross-correlation" (if the temporal information is separated in two images). This latter technique is usually preferred, due to its better stability against noise.The image frames are interrogated by the computation of the spatial cross-correlation in an $M \times N$ interrogation region:

$$R(\boldsymbol{d}) = \frac{1}{\|\mathscr{W}(\boldsymbol{x})\|} \sum_{\boldsymbol{y} \in \mathscr{W}(\boldsymbol{x})} I_1(\boldsymbol{y}) \times I_2(\boldsymbol{y} + \boldsymbol{d}(\boldsymbol{x})), \quad (1)$$

where I_1 and I_2 are the first and second discrete image frames, $\mathscr{W}(\boldsymbol{x})$ being a window centered on the point $\boldsymbol{x}$. The motion associated to the centre of the interrogation window $\boldsymbol{d}(\boldsymbol{x}) = (u(\boldsymbol{x}),v(\boldsymbol{x}))$ corresponds to a peak of the correlation surface.

Three main options are available to compute the correlation surface Eq. 1:

1. Direct computation: this method requires $(M \times N)^2$ multiplications and additions for an $(M \times N)$ interrogation window and is thus expensive in computation time;
2. Computation in the Fourier domain: this technique is used to accelerate the previous processing and to localize easily the correlation peak. Unfortunately, one difficulty of this approach is the lack of flexibility between the Fourier domain and the physical one, especially for post-processing treatment;
3. Computation in the spectral domain with physical post-processing using the Wiener–Khintchine theorem that permits a fast come back in the physical domain

As they lead to real time computations, the second and third options (computation in the Fourier space) are mainly used in PIV. Let us notice that to prevent from aliasing artefacts, Nyquist criteria must be respected: the considered displacement $\boldsymbol{d}$ is then such that $\boldsymbol{d} < (N/2, M/2)$ pixels. Hence, if necessary, an underestimation of the velocity magnitude is commonly performed by growing up the size of the interrogation window or by decreasing the time interval between two laser pulses. This manipulation may affect significantly the quality of the estimated motion field and a compromise has to be generally defined between a direct computation which does not have such restrictions and a fast computation in the Fourier space (McKenna and McGillis 2002).

Another difficulty inherent to correlation methods lies in the discrete data nature. As a matter of fact, with such approaches the estimated displacement vector is intrinsically discretized on the image grid (i.e. vectors of the type $\boldsymbol{d} = u \times \text{pix}, v \times \text{pix}$), where u and v are integers and pix is the pixel size). Infinitesimal brightness variation can indeed not be identified. This results in the well known "peak-locking" effect which spoils the accuracy of the velocity measurement. Many studies have been done to attenuate this phenomenon. One possibility consists in increasing particle size (which effective particle image size must be two or three pixels) or to pay a particular attention to the correlation maxima localization (by sound interpolations for example). Several methods have been proposed to provide "sub-pixel" accuracy (Lourenco and Krothapalli 1995; Willert and Gharib 1991).

Actually, many extensions of the basic cross-correlation principle have been proposed to improve the estimation quality in terms of dynamic range, accuracy and spatial resolution. For example Scarano and Reithmuller (2000) and Lecuona et al. (2002) used an iterative prediction of the unknown velocity in the estimation scheme, whereas Lourenco and Krothapalli (2000) or

Wereley and Meinhart (2001) directly modified the correlation criterion, using a central difference approximation (of second order) instead of a forward difference approximation (of first order) as commonly done. One can also note that the use of a super-resolution technique as in Nogueira et al. (2001) allows an uncertainty reduction and attenuates the effect of peak-locking.

2.3 Discussion

Many studies on cross-correlation methods have been done and many methods enabling to extract relevant motion information are available. Even if the principle of correlation techniques enables to extract only displacement vectors on the image lattice, many extended methods have been proposed to achieve "sub pixel" accuracy. All these correlation techniques share nevertheless some common limitations which prevents a comfortable use (Lourenco and Krothapalli 2000):

1. Due to the finite size of the interrogation area and particle drop out, a "*loss of pairing*" may alter the estimation. In this case, the maximum of correlation does not correspond to the actual motion. The definition of the size of the interrogation window is indeed very problematic to extract a relevant motion in accordance with the observed phenomenon;
2. The existence of "*velocity and speeding gradient in the interrogation region*" introduces a bias towards the lower displacements and higher seeded sub-regions as a result of the more frequent pairings. For large interrogation windows, this is very problematic. It is nevertheless important to note that this can be (at least partially) overcome using variable size windows and deformable grids (Scarano and Reithmuller 2000);
3. Due to its statistical nature, only the "most probable" displacement is extracted for each interrogation window.

All these limitations can hardly be avoided as they are intrinsically linked to the discrete and local nature of correlation methods.

Optical-flow approaches, originally introduced by Horn and Schunck (1981), enable to extract in a natural way a *dense* motion field (i.e. one vector per pixel). Such techniques take into account the whole image to estimate a vectorial continuous function representing the velocity field. As a consequence they are intrinsically able to avoid the difficulties mentioned above. The idea which consists of using optical-flow methods for PIV images appears then very attractive. Unfortunately such techniques designed for computer vision applications have also some limitations, which prevents their direct use in an experimental fluid mechanics context.

In the following section, we give more details on the basis of generic optical-flow schemes. We then discuss their limitations with respect to fluid image sequences and present our extension of these techniques, specifically dedicated to fluid flows velocity measurements.

3 Optical-flow scheme

Obtaining the *optical flow* consists in estimating a dense motion field from two consecutive images. As previously mentioned, many methods have been proposed in the last two decades to estimate such an optical flow. Most of them are based on the seminal work of Horn and Schunck (1981). In this section, optical-flow methods will then refer to this latter definition. It is nevertheless important to point out that some authors propose reliable optical-flow computations not based on Horn and Schunck (1981), especially for PIV images in Quénot et al. (1998) where the authors use dynamic programming and orthogonal algorithms. The reader will find in Barron et al. (1994) a survey of different methods for computing optical flow (differential techniques, region based matching, energy based methods and phase based techniques).

3.1 Generic optical-flow estimator

The most accurate techniques to address the generic problem of estimating the apparent motion from image sequences are based on the seminal work by Horn and Schunck (1981). These techniques are based on the minimization of a global cost function $\mathscr{H}$ composed of two terms. The first one, named "observation term", is derived from a *brightness constancy* assumption and assumes that a given point keeps the same intensity along its trajectory. It is expressed through the well known *optical flow constraint equation* (OFCE):

$$\mathscr{H}_{\text{obs}}(E,\boldsymbol{v}) = \iint_{\Omega} f_1\left[\nabla E(\boldsymbol{x},t)\boldsymbol{v}(\boldsymbol{x},t) + \frac{\partial E(\boldsymbol{x},t)}{\partial t}\right]\mathrm{d}\boldsymbol{x}, \qquad (2)$$

where $\boldsymbol{v}(\boldsymbol{x},t) = (u,v)^T$ is the unknown velocity field at time t and location $\boldsymbol{x} = (x,y)$ in the image plane Ω, $E(\boldsymbol{x},t)$ is the image brightness, viewed for a while as a continuous function. This first term relies on the assumption that the visible points conserve roughly their intensity in the course of a small displacement.

$$\frac{\mathrm{d}E}{\mathrm{d}t} = \nabla E\boldsymbol{v} + \frac{\partial E}{\partial t} \approx 0. \qquad (3)$$

The associated penalty function f_1 is often the L_2 norm. However, better estimates are usually obtained by choosing a "softer" penalty function (Black 1994; Mémin and Pérez 1998). Such functions, arising from robust statistics (Huber 1981), limit the impact of the many locations where the brightness constancy assumption does not hold, such as on occlusion boundaries. Appendix B briefly presents robust estimators used in this paper.

This single (scalar) observation term does not allow to estimate the two components u and v of the velocity. In order to solve this ill-posed problem, it is common to employ an additional smoothness constraint $\mathscr{H}_{\text{reg}}$. Usually, this second term enforces a spatial smoothness coherence of the flow field. It relies on a contextual

assumption which enforces a spatial smoothness of the solution. This term usually reads:

$$\mathscr{H}_{\text{reg}}(\boldsymbol{v}) = \iint_{\Omega} f_2[|\nabla u(\boldsymbol{x},t)| + |\nabla v(\boldsymbol{x},t)|], \tag{4}$$

As with the penalty function in the data term, the penalty function f_2 was taken as a quadratic in early studies, but a softer penalty is now preferred in order not to smooth out the natural discontinuities (boundaries,...) of the velocity field (Black 1994; Cohen and Herlin 1999; Kornprobst et al. 1999; Mémin and Pérez 1998). Based on Eqs. 2 and 4, the estimation of motion can be done by minimizing:

$$\begin{aligned}\mathscr{H}(E,\boldsymbol{v}) &= \mathscr{H}_{\text{obs}}(E,\boldsymbol{v}) + \alpha\mathscr{H}_{\text{reg}}(\boldsymbol{v}) \\ &= \iint_{\Omega} f_1\left[\nabla E(\boldsymbol{x},t)\boldsymbol{v}(\boldsymbol{x},t) + \frac{\partial E(\boldsymbol{x},t)}{\partial t}\right]\mathrm{d}\boldsymbol{x} \\ &\quad + \alpha\iint_{\Omega} f_2[|\nabla u(\boldsymbol{x},t)| + |\nabla v(\boldsymbol{x},t)|],\end{aligned} \tag{5}$$

where $\alpha > 0$ is a parameter controlling the balance between the smoothness constraint and the global adequacy to the observation assumption.

Due to its differential nature, the relation in Eq. 2 is only defined for infinitesimal displacements. To handle large displacements it is common to use the expression Eq. 2 of the brightness conservation in an integrated way:

$$E(\boldsymbol{x} + \boldsymbol{d}(\boldsymbol{x}), t + \Delta t) - E(\boldsymbol{x}, t) \approx 0, \tag{6}$$

where Δt is the temporal sampling rate and $\boldsymbol{d}(\boldsymbol{x})$ is the *displacement* from time t to $t + \Delta t$ of the point located at position $\boldsymbol{x}$ at time t. This new form, valid whatever the magnitude of $\boldsymbol{d}(\boldsymbol{x})$ be, is however highly nonlinear in the unknown vector. As a consequence, almost all studies resort to a succession of linearizations around a previous estimate $\tilde{\boldsymbol{d}}(\boldsymbol{x})\tilde{\boldsymbol{d}}(\boldsymbol{d})\tilde{\boldsymbol{d}}(\boldsymbol{x})$ $(\boldsymbol{d}(\boldsymbol{x}) = \tilde{\boldsymbol{d}}(\boldsymbol{x})\tilde{\boldsymbol{d}}(\boldsymbol{d})\tilde{\boldsymbol{d}}(\boldsymbol{x}) + \Delta\boldsymbol{d}(\boldsymbol{x}))$ embedded within a multiresolution scheme (using a bilinar interpolation for the projection). The new cost-function to be minimized with respect to the displacement increment $\Delta\boldsymbol{d}$ reads then:

$$\begin{aligned}\mathscr{H}(E,\Delta\boldsymbol{d}) = \iint_{\Omega} f_1\big[&\nabla E(\boldsymbol{x} + \tilde{\boldsymbol{d}}(\boldsymbol{x}), t + \Delta t)\Delta\boldsymbol{d}(\boldsymbol{x}) \\ &+ E(\boldsymbol{x} + \tilde{\boldsymbol{d}}(\boldsymbol{x}), t + \Delta t) \\ &- E(\boldsymbol{x}, t)\big] + \alpha f_2\big[\big|\nabla(\tilde{\boldsymbol{d}} + \Delta\boldsymbol{d})(\boldsymbol{x})\big|\big].\end{aligned} \tag{7}$$

The associated successive minimizations are usually performed using efficient iterative methods (Mémin and Pérez 1998, 2002).

It is important to outline that such an estimator defined as the minimizer of $\mathscr{H}$ is generic. It is only based on the assumption of luminance conservation and of first-order spatial smoothness of the motion. Even if this kind of estimator has been successfully used for fluid motion (Bannehr et al. 1996; Cohen and Herlin 1999; Larsen et al. 1998; Mémin and Pérez 1999; Ruhnau et al. 2005; Wallace and Foss 1995), the underlying assumptions are far from being sound hypothesis for such an applicative domain. As a matter of fact, image sequences representing fluid phenomena exhibit areas where the luminance function undergoes high temporal variations along the motion. These areas are often the centre of tridimensional motions that cause the appearance or the disappearance of fluid matter within the bidimensional visualization plane. These regions are in addition associated to divergent motions which influence greatly the shape of the velocity field in large surrounding areas. An accurate estimation of the 2D apparent motion in such regions is therefore of the highest importance and is hardly possible with the optical-flow constraint.

3.2 Fluid dedicated optical-flow estimator

In a recent paper Corpetti et al. (2002) proposed an optical-flow technique specifically dedicated to image sequences depicting fluid flow phenomenona. This specialized optical-flow estimator relies on an adaptation of the functional data model and smoothness term.

3.3 Continuity equation and data model

Instead of sticking to the intensity conservation assumption, the data model that has been considered relies on the continuity equation:

$$\frac{\partial\chi}{\partial t} + \mathrm{div}(\chi\boldsymbol{v}) = 0, \tag{8}$$

where χ denotes the density of the fluid, $\boldsymbol{v}$ its 3D velocity and $\mathrm{div}\boldsymbol{v} = \frac{\partial u}{\partial x} + \frac{\partial v}{\partial y} + \frac{\partial w}{\partial z}$ stands for the divergence of the vector field $\boldsymbol{v} = (u,v,w)$. Simple manipulations yield the alternative writing:

$$\frac{\mathrm{d}\chi}{\mathrm{d}t} + \chi\mathrm{div}\boldsymbol{v} = 0. \tag{9}$$

When the divergence of the 3D apparent flow vanishes, this equation is of the same form as the 2D optical flow constraint on luminance. The continuity equation, originally introduced in Schunk (1984) as a data model for motion estimation of intensity time varying images, has been since incorporated in several works. It has been considered in the context of fluid imagery either for satellite meteorological images (Béréziat et al. 2000; Corpetti et al. 2002; Zhou et al. 2000) or for experimental fluid mechanics (Wildes et al. 1997). It has also been introduced in medical imaging domain to recover 3D deformation fields of the heart (Song and Leahy 1991) or to analyse blood flow (Amini 1994). In all these cases, this model has been proved to represent an alternative to standard luminance constancy assumption.

The use of continuity equation for image sequences analysis relies on two hypotheses. First, the luminance function is assumed to be directly related to a passive quantity transported by the fluid. Secondly, the continuity equation which holds in 3D, is assumed to hold as

well for the bidimensional motion field captured by the image sequence. This latter assumption has been theoretically established in the case of transmittance imaging by Fitzpatrick (1988) and extended by Wildes et al. (1997). The first assumption is difficult to validate, especially in meteorological images due to the complexity and the heterogeneity of the underlying physical processes. Nevertheless, as shown by several works, the use of the continuity equation in the case of meteorological data is appealing (Béréziat et al. 2000; Zhou et al. 2000). As the brightness consistency is obviously not verified in that type of images, the continuity equation provides an interesting alternative data model. Instead of expressing a point-wise conservation of the luminance along the motion, this alternative model assumes the conservation of the total luminance of any moving element of the image. This constraint reads:

$$\frac{\mathrm{d}E}{\mathrm{d}t} + E\mathrm{div}\boldsymbol{v} = 0. \tag{10}$$

However, as OFC-based data models, a data model based on the continuity equation is highly sensitive to the presence of noise and is very likely not to hold everywhere. Also, due to its differential nature, the continuity equation is not valid in case of large displacements. In fact, this equation concerns the *velocity* $\boldsymbol{v}$ and not *displacement* (Nomura et al. 1991). Unlike the brightness constancy expressed as $E(\boldsymbol{x}+\boldsymbol{d}(\boldsymbol{x}),t+\Delta t)-E(\boldsymbol{x},t)=0$, which is explicitly based on displacement, the continuity Eq. 10, as it stands, cannot serve as the basis of an incremental data-model embedded in hierarchical estimation schemes. To cope with this problem, let us assume that the velocities are constant between the instants t and $t+\Delta t$. In that case, Eq. 10 constitutes a simple first-order differential equation which can be integrated from time t to time $t+\Delta t$ along trajectories. Setting $\Delta t=1$ for notational convenience, and incorporating the integral constraint thus obtained in a robust penalty function yields a new data term:

$$\mathscr{H}_{\mathrm{obs}}(\boldsymbol{d}) = \iint_{\Omega} f_1(E(\boldsymbol{x}+\boldsymbol{d}(\boldsymbol{x}),t+1)\exp(\mathrm{div}\boldsymbol{d}(\boldsymbol{x})) - E(\boldsymbol{x},t))\mathrm{d}\boldsymbol{x}, \tag{11}$$

where $\boldsymbol{d}(\boldsymbol{x})$ is now the displacement from time t to $t+\Delta t$ of a point located at position $\boldsymbol{x}$ at time t. This form is nonlinear with respect to the unknown velocity field $\boldsymbol{d}$ to estimate. As mentioned in Sect. 3.1, we then linearize Eq. 11 around a crude solution $\tilde{\boldsymbol{d}}$ and embed it in a multiresolution scheme. The new linearized observation term based on the integrated continuity equation (ICE) is:

$$\mathscr{H}_{\mathrm{obs}}(\Delta\boldsymbol{d}) = \iint_{\Omega} f_1\big[\exp(\mathrm{div}\tilde{\boldsymbol{d}}(\boldsymbol{x}))\big((\tilde{E}(\boldsymbol{x})\nabla\mathrm{div}\tilde{\boldsymbol{d}}(\boldsymbol{x}) + \nabla\tilde{E}(\boldsymbol{x})).\,\Delta\boldsymbol{d}(\boldsymbol{x}) + \tilde{E}(\boldsymbol{x})\big) - E(\boldsymbol{x})\big]\mathrm{d}\boldsymbol{x}, \tag{12}$$

where $\Delta\boldsymbol{d}=\boldsymbol{d}-\tilde{\boldsymbol{d}}$, and we introduce the compact notation $\tilde{E}(\boldsymbol{x})=E(\boldsymbol{x}+\tilde{\boldsymbol{d}}(\boldsymbol{x}),t+\Delta t)$. We now turn to the definition of the smoothness prior to be used in conjunction with this new data energy term.

3.4 Second-order Div–Curl regularization

By using Euler–Lagrange conditions of optimality, it is readily demonstrated (see Appendix A) that the standard first-order regularization functional:

$$\mathscr{H}_{\mathrm{reg}}(\boldsymbol{v}) = \iint_{\Omega} |\nabla u(\boldsymbol{x})|^2 + |\nabla v(\boldsymbol{x})|^2 \mathrm{d}\boldsymbol{x}$$

is equivalent from the minimization point of view, to the so-called *div–curl* regularization functional (Suter 1994):

$$\mathscr{H}_{\mathrm{reg}}(\boldsymbol{v}) = \iint_{\Omega} \big(\mathrm{div}^2\boldsymbol{v}(\boldsymbol{x}) + \mathrm{curl}^2\boldsymbol{v}(\boldsymbol{x})\big)\mathrm{d}\boldsymbol{x}, \tag{13}$$

where $\mathrm{div}\boldsymbol{v}=\frac{\partial u}{\partial x}+\frac{\partial v}{\partial y}$ and $\mathrm{curl}\boldsymbol{v}=\frac{\partial v}{\partial x}-\frac{\partial u}{\partial y}$ are, respectively, the divergence and the vorticity of the motion field $\boldsymbol{v}=(u,v)$.

A first-order regularization therefore penalizes the amplitude of both the divergence and the vorticity of the vector field. For fluid motion estimation, this does not seem appropriate since the apparent velocity field normally exhibits compact areas with high values of vorticity and/or divergence. In addition, an underestimation of the divergence would be all the more problematic in our case, because the data model includes an explicit use of this quantity. For these reasons, it seems more appropriate to rely on a second-order div–curl regularization (Gupta and Prince 1996; Suter 1994):

$$\mathscr{H}_{\mathrm{reg}}(\boldsymbol{d}) = \iint_{\Omega} \Big(|\nabla\mathrm{div}\boldsymbol{d}(\boldsymbol{x})|^2 + |\nabla\mathrm{curl}\boldsymbol{d}(\boldsymbol{x})|^2\Big)\mathrm{d}\boldsymbol{x}. \tag{14}$$

This regularization tends to preserve the divergence and the vorticity of the displaced motion field $\boldsymbol{d}$ to estimate. Nevertheless, this new term is more difficult to implement. As a matter of fact, the associated Euler–Lagrange equation is composed with two fourth order coupled PDE's, which are tricky to solve numerically. In order to simplify the problem we have considered a modified smoothness term based on the same principles. This new smoothness term has been built by introducing auxiliary functions in the original second-order div–curl regularization:

$$\mathscr{H}_{\mathrm{reg}}(\boldsymbol{d},\xi,\zeta) = \alpha\iint_{\Omega} |\mathrm{div}\boldsymbol{d}-\xi|^2 + \lambda\|\nabla\xi\|^2 + \alpha\iint_{\Omega} |\mathrm{curl}\boldsymbol{d}-\zeta|^2 + \lambda\|\nabla\zeta\|^2. \tag{15}$$

The new auxiliary scalar functions ξ and ζ can respectively be seen as estimates of the divergence and the vorticity of the unknown motion field, and λ is a positive parameter. The first part of each integral encourages the displacement to comply with the current divergence and vorticity estimates ξ and ζ, through a quadratic goodness-of-fit enforcement. The second part equips the divergence and the vorticity estimates with a first-order regularization favoring piece-wise smooth configurations. Getting rid of the auxiliary scalar fields ξ and ζ in (15) (by setting $\xi = \mathrm{div}\boldsymbol{d}$ and $\zeta = \mathrm{curl}\boldsymbol{d}$) would amount to the original *second-order* div–curl regularization (14).

From a computational point of view, regularizing functional Eq. 15 only implies the numerical resolution of first-order PDE's at the expense of course of new variables. This reformulation authorizes to use nearly the same optimization strategy involved in generic optical-flow estimator. Interested readers may refer to Corpetti et al. (2002) to get precise descriptions on the optimization strategy and on associated numerical implementation issues.

3.5 Minimization issue

We now turn to the minimization issue of the whole energy function $\mathscr{H} = \mathscr{H}_{\mathrm{obs}} + \alpha\mathscr{H}_{\mathrm{reg}}$. Two main sets of variables have to be estimated. The first one is the motion field $\boldsymbol{d}$, and the second one consists in the two scalar fields ξ and ζ. The estimation is conducted alternatively by minimizing $\mathscr{H}_{\mathrm{obs}} + \alpha\mathscr{H}_{\mathrm{reg}}$ with respect to $\boldsymbol{d}$, ξ and ζ:

$$\min_{\Delta\boldsymbol{d},\xi\zeta} \mathscr{H}_{\mathrm{obs}}(\Delta\boldsymbol{d}) + \alpha\mathscr{H}_{\mathrm{reg}}(\Delta\boldsymbol{d},\xi,\zeta), \tag{16}$$

For the motion field $\boldsymbol{d}$, the use of a robust penalty function in the observation term yields to an iteratively re-weighted least squares minimization with the estimation of outliers data z (see Appendix B). Concerning ξ and ζ, we have a linear least-square problem. A Gauss-Seidel solver was used for all linear least-square minimizations. The process is considered to be finished when the relative change in the L_2-norm of $\Delta\boldsymbol{d}$ is below 1%.

The minimization process is summarized below:

- $\tilde{\boldsymbol{d}} \equiv 0$
- From coarsest to finest resolution do
  - $\Delta\boldsymbol{d} \equiv 0$, $\xi \equiv 0$, $\zeta \equiv 0$, $z \equiv 0$
  - Until convergence do[a] [b] [c]
    - Estimation of $\Delta\boldsymbol{d}$ with robust functions :

$$\begin{aligned}\Delta\boldsymbol{d} \leftarrow\ & GS\Big(\iint_\Omega z(\boldsymbol{x})g^2(\Delta\boldsymbol{d}) \\ & +\alpha|\mathrm{div}\tilde{\boldsymbol{d}}(\boldsymbol{x}) + \mathrm{div}\Delta\boldsymbol{d}(\boldsymbol{x}) - \xi(\boldsymbol{x})|^2 \\ & +\alpha|\mathrm{curl}\tilde{\boldsymbol{d}}(\boldsymbol{x}) + \mathrm{curl}\Delta\boldsymbol{d}(\boldsymbol{x}) - \zeta(\boldsymbol{x})|^2 d\boldsymbol{x}\Big)\end{aligned}$$

    - Update $z(\boldsymbol{x})$ (see appendix B for details):

$$z(\boldsymbol{x}) \leftarrow \tau_1 \exp -\tau_1 g^2(\Delta\boldsymbol{d})$$

    - Estimation of ξ :

$$\begin{aligned}\xi \leftarrow\ & GS\Big(\iint_\Omega |\mathrm{div}\tilde{\boldsymbol{d}}(\boldsymbol{x}) + \mathrm{div}\Delta\boldsymbol{d}(\boldsymbol{x}) - \xi - (\boldsymbol{x})|^2 \\ & +\lambda\iint_\Omega \|\boldsymbol{\nabla}(\xi(\boldsymbol{x})\|^2 d\boldsymbol{x}\Big)\end{aligned}$$

    - Estimation of ζ :

$$\begin{aligned}\zeta \leftarrow\ & GS\Big(\iint_\Omega |\mathrm{curl}\tilde{\boldsymbol{d}}(\boldsymbol{x}) + \mathrm{curl}\Delta\boldsymbol{d}(\boldsymbol{x}) - \zeta(\boldsymbol{x})|^2 \\ & +\lambda\iint_\Omega \|\boldsymbol{\nabla}\zeta(\boldsymbol{x})\|^2 d\boldsymbol{x}\Big)\end{aligned}$$

- If not finest resolution, pass $\tilde{\boldsymbol{d}} \leftarrow \tilde{\boldsymbol{d}} + \Delta\boldsymbol{d}$ to next resolution.
- If finest resolution, $\boldsymbol{d} \leftarrow \tilde{\boldsymbol{d}} + \Delta\boldsymbol{d}$.

(17)

[a] Convergence is reached when the relative change in the L_2-norm of $\Delta\boldsymbol{d}$ is below 1%.

[b] $g(\Delta\boldsymbol{d})$ denotes $\exp(\mathrm{div}\tilde{\boldsymbol{d}}(\boldsymbol{x}))\big((\tilde{E}(\boldsymbol{x})\nabla\mathrm{div}\tilde{\boldsymbol{d}}(\boldsymbol{x}) + \nabla\tilde{E}(\boldsymbol{x}))\cdot\Delta\boldsymbol{d}(\boldsymbol{x}) + \tilde{E}(\boldsymbol{x})\big) - E(\boldsymbol{x})$.

[c] "$GS()$" denotes one Gauss-Seidel iteration on the quadratic form under consideration.

Let us now have a particular attention to the minimization w.r.t the motion field $\Delta \boldsymbol{d}$ (first Eq. 17). For better and faster convergence, the minimization with respect to the incremental displacement field $\Delta \boldsymbol{d}$ at a given resolution is performed using the coarse-to-fine multi-parametric multigrid framework technique introduced in Mémin and Pérez (1998).

More precisely, the motion is constrained to be piecewise-parametric relatively to an image partition which becomes finer and finer. At a "grid" level (named ℓ), the pixel grid is partitioned in blocks B_n^ℓ of size $2^\ell \times 2^\ell$, and the increment field is constrained to satisfy a chosen parametric model. In practice, until the penultimate grid level, the affine parametrization is chosen (i.e: $(u,v)^T = \begin{bmatrix} 1 & x & y & 0 & 0 & 0 \\ 0 & 0 & 0 & 1 & x & y \end{bmatrix} \Theta$). The last level $\ell = 0$ corresponds to the pixel grid itself: when it is finally reached, no parametric constraint applies anymore. At each given level, the cost terms to be minimized must be rewritten in function of the parameter vectors (Θ). This symbolic rewriting is explained in Mémin and Pérez (1998).

The estimation at the coarsest grid-level is fast because the space of solutions is of reduced dimension. It serves as a reliable initialization for the next level, yielding to this new computation more efficiency, and so on until the pixel grid itself.

The combination of the multiresolution and the multigrid techniques partly makes possible to prevent from stopping the process of minimization in a local minimum.

More details of the minimization issues can be seen in Corpetti et al. (2002).

4 Experimental details

4.1 VSJ standard image-pairs

The visualization society of Japan (VSJ) developed in 1999 PIV standard images and PIV guide tools in order to popularize the PIV techniques. Within this project, many synthetic PIV image sequences called "standard images", were generated along with the corresponding ground truth velocity vector fields in a wide variety of controlled conditions (Okamoto et al. 2000). They are available on the internet. The parameters of the eight standard situations tested in this paper are listed in Table 1 and represent: the number N of particles that are present in the images, the particle diameter D_m associated to its standard deviation D_s, the average image velocity v_m and the out-of-plane velocity w_m. Compared to image pair #1, the pairs #2 and #3 differ only with respect to the magnitude of the flow field; the image pairs #4 and #5 have only different number of particle; the pairs #6 and #7 have particles with a different diameter while the pair #8 has a high out of plane velocity.

Some results on these images are available in the literature (Quénot 1999; Ruhnau et al. 2005). We used the relative L_1 norm error (L_1 norm of the difference between the correct and computed velocities in pixels/frame divided by the average in-plane velocity) to compare the different motion fields.

4.2 Plane turbulent mixing layer

The mixing layer studied here has been generated in a closed circuit, subsonic wind tunnel R300 of the Centre d'Études Aérodynamiques et Thermiques, University of Poitiers, France (CEAT). This wind tunnel has a square test section of cross-sectional dimensions 300 mm×300 mm and length 2 m, with a contraction ratio of ten. The one stream blow generated by a fan is divided by a splitter plate in two separated streams flowing through two different head loss devices, followed by fine mesh screens, and are jointly released at the end of the splitter plate to give a two-stream flow with low initial turbulence level. Tripping wire were used on both sides of the splitter plate to ensure a rapid and uniform transition of the boundary layer well upstream of the trailing edge. Hence, the mixing layer is initially turbulent. Wind-tunnel ceiling was tilted to achieve a negligible streamwise pressure gradient. For more details about the facility, the reader can refer to Heitz (1999). The velocity ratio of the two streams $r = U_a/U_b$ ($U_a = 9$ m s^{-1} and $U_b = 6$ m s^{-1}) was 0.67 with an average advective velocity $U_m = (U_a + U_b)/2$ of 7.5 m s^{-1}. The turbulence intensity corresponding to free stream velocity is less than 0.3%. The location of the origin of the x axis corresponds to the position where the vorticity thickness of the mixing layer δ_ω equaled 15 mm and was found 240 mm downstream of the trailing edge of the splitter plate. In all the figures this value was employed to reduce x and y coordinates.

4.3 Wake of a circular cylinder

The experiments in the near wake of a circular cylinder were carried out in a small opened wind tunnel of the Cemagref (Center of Rennes, France), having a test section 142 mm wide 142 mm high, and 1,100 mm long. The wind tunnel consists of a blower supplying air to a conditioning system composed of a honeycomb and a porous media (foam) followed by a 2:1 contraction, which provided a free-stream uniformity and a turbulence intensity less than 0.1%. The flow velocity was 4.5 m s^{-1}. The circular cylinder had a cross-sectional diameter $D = 10$ mm and a length $L = 142$ mm giving an aspect ratio of $L/D = 14.2$. The value of the Reynolds number based on the diameter D was Re = 3,000. The cylinder was mounted vertically and no end plates were used to limitate end effects.

4.4 PIV settings

Two different PIV systems were used for these two experiments.

For the mixing layer the illumination setup comprised an Nd:YAG double-pulses laser system (Quantel) with an output energy of 30 mJ per pulse at a green wavelength $\lambda = 532$ nm. The flow was seeded with particles of oil. The spray generator was located downstream of the test section in the closed loop of the wind tunnel, to ensure good homogeneity of the seeding in the view plane. The images were captured by a CCD Kodak camera (type 700) of 1,008×984 pixels resolution and 8 bit dynamic range. The camera was placed so that the middle-height of the image corresponded to the location of the splitter plate, and so that the vorticity thickness of the mixing layer (δ_ω) at the inlet of the image was equal to 15 mm. The image size in the physical space was $L_x \times L_y = 84.5\times82.5$ mm$^2 = 5.6\,\delta_\omega\times5.5\delta_\omega$. The laser pulse rate was adjustable up to 20 Hz but the acquisition frequency was limited to 15 Hz by the camera frame rate. The pulse delay was fixed at $\Delta t = 50$ μs in order to keep particle displacements in an adequate range for PIV. Synchronization of the camera apertures with the laser pulses was achieved using LaVision hardware system. The software of LaVision, Davis, was also used to calculate the cross-correlation of the two pairs of grey level images acquired by the camera. For comparison with optical flow results two interrogation procedures, named PIV I and PIV II, respectively, were applied. A 32×32 pixels interrogation window with 50% overlap was used for PIV I, leading to a grid spacing of 16×16 pixels (1.34×1.34 mm^2), and a multipass technique with two refinement steps and 50% overlap was used for PIV II to obtain interrogation regions as small as 16×16, yielding a grid spacing of 8×8 pixels (0.67×0.67 mm^2 i.e. $0.05\times0.05\delta_\omega^2$).

For the wake of the circular cylinder the illumination setup comprised an Nd:YAG double-pulses laser system (New Wave) with an output energy of 30 mJ per pulse at a green wavelength $\lambda = 532$ nm. The flow was seeded with particles of oil. The spray generator was located upstream of the blower, to ensure good homogeneity of the seeding in the view plane. The images were captured by a CCD LaVision camera of 1,280× 1,024 pixels resolution and 12 bit dynamic range. The image size in the physical space was $L_x \times L_y = 98.7\times83.4$ mm^2 $9.9D\times 8.3D$. The laser pulse rate was adjustable up to 20 Hz but the acquisition frequency was limited to 15 Hz by the camera frame rate. The pulse delay was fixed at $\Delta t = 69$ μs in order to keep particle displacements in an adequate range for PIV. Synchronization of the camera apertures with the laser pulses was achieved using LaVision hardware system. The software of LaVison, Davis, was also used to calculate the cross-correlation of the two pairs of grey level images acquired by the camera. A multiphase technique with refinement steps was used to obtain interrogation regions as small as 16×16 pixels, leading to a grid spacing of 12×12 pixels (0.93×0.93 mm^2 i.e. $0.093\times0.093D^2$).

Both instantaneous and averaged quantities were employed to represent the flow structure. Mean quantities were computed with the whole sequence of 520 and 540 instantaneous vector fields for the mixing layer and the circular cylinder wake, respectively.

4.5 Optical-flow settings

For the optical-flow approach, regularization parameters used are $\alpha = 300$ and $\lambda = 300$. For the penalty function f_1, we choose the Leclerc penalty function $f_1(x) = 1-\exp(-\tau_1 x^2)$ instead of the quadratic one because of the non-systematic correspondence between the brightness intensity and particle concentration. Parameter τ_1 has then to be set and we choose its value as $\tau_1 = 1.6$.

The number of resolution level and grid level is 3. The choice of these three parameters was done initially on synthetic images (Corpetti et al. 2002). The same set of parameters values was kept whatever the input data were. For the f_2 penalty function dedicated to the div–curl regularization, we chose a quadratic penalization function owing to the fact that we have a physical spatial-continuity both on the divergence and the vorticity of the flow.

Optical-flow technique yields a grid spacing of 1×1 pixel. Therefore the values of spatial resolution in the plane of the laser sheet, for the mixing layer and the circular cylinder wake, were 0.08×0.08 mm^2 i.e. $0.006\times0.006\delta_\omega^2$ and 0.08×0.08 mm^2 i.e. $0.008\times0.008D^2$, respectively.

4.6 Vorticity measurement

Parameter ζ issued from the motion estimator Eq. 15 is a measure of the vorticity. It is computed via a simple finite difference scheme $(\mathrm{curl}(\boldsymbol{d}(x,y)) = (v_{x+1,y} - v_{x-1,y})/(2\Delta_x) - (u_{x,y+1} - u_{x,y-1})/(2\Delta_y))$. For the mixing layer experience, this parameter gave a vorticity map that was very noisy. We can naturally wonder whether this noise was introduced by the optical-flow scheme. But when we analysed the second experiment (the circular cylinder),

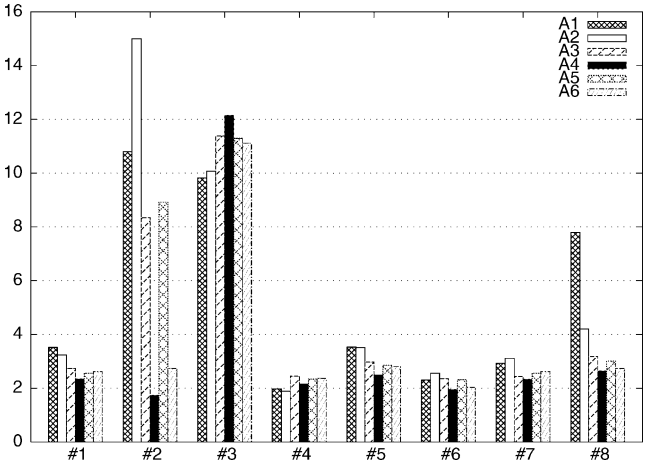

Fig. 1 Average relative L_1 error of six algorithms. From left to right (and top to bottom in the legend): **A1**: ODP from Quénot (1999); **A2**: VOF from Ruhnau et al. (2005); **A3**: RMM from Mémin and Pérez (1998); **A4:** The proposed approach; **A5:** The proposed ICE associated to a first-order regularization and **A6**: The usual OFCE associated to the presented Div–Curl regularization

the vorticity obtained by ζ was significantly less disturbed.

Concerning the data, an 8 bit CCD Kodak camera was used for the mixing layer experiment whereas a 12 bit CCD La Vision camera was employed for the study of the wake of the circular cylinder. The latter camera is known to have a Pelletier cooling system which reduces the source of noise due to thermal effects. This suggests that the noisy vorticity of the mixing layer was due to the measurement noise in the input images and that the proposed estimator was able to capture it.

Hence, to reduce noise on the vorticity for the mixing layer experiment, we decided to use the more sophisticated method presented in Raffel et al. (2000). The average vorticity was estimated within an enclosed area of 3×3 pixels by calculating the local circulation around this area. Indeed, the error in the measurement of the vorticity depends on the truncation error associated with the finite difference scheme used, and on the measurement uncertainty, ε, which is directly proportional to the grid spacing, that is $\varepsilon/\Delta x$ (Lourenco and Krothapalli 1995; Raffel et al. 2000). For the second experiment, the classic finite difference scheme of order 2 was used both for PIV and optical flow.

5 Results for the VSJ standard images

Figure 1 shows the average L_1 relative error of six algorithms: **A1**, the orthogonal dynamic programming (ODP) issued from Quénot 1999; **A2**, the variational optical flow (VOF) implementation of Horn and Schunck presented in Ruhnau et al. 2005; **A3**, the robust multiresolution/multigrid (RMM) implementation of Horn and Schunck presented in Mémin and Pérez 1998; **A4**, the proposed approach; **A5**, the proposed integrated continuity equation (ICE) associated to a first order regularization and **A6**, the usual OFCE constraint associated to the presented Div–Curl regularization.

Compared to other methods the proposed approach gives better results for cases {#1,#2, #5,#6,#7,#8 }.

Results on case #4 are good for all techniques with slightly better results for estimators **A1** and **A2**. Nevertheless, as expected, the div–curl and ICE options (**A4**) are better than others combinations (**A3**, **A5** and **A6**) with the same implementation method. Concerning case #3 (where the motion range is low), all estimators give important errors on the motion field. The bad results obtained with the proposed technique can be explained by (1) the multiresolution process (which may introduce errors due to bilinear interpolation is not necessary here); (2) by the div–curl regularization (which seems to introduce more artefacts than the others methods) and (3) by the ICE constraint (the out of plane velocity is very small here and this option is likely to introduce a divergent motion at each change of illumination). Nevertheless, in practice, it is often possible to have an idea of the magnitude of the motion and to adapt parameters.

Case #2 is very interesting: referring to Table 1, one can see that the velocity is very important (and as a consequence, the underlying vorticity too). Even if most of the presented approaches have a multiresolution implementation, all estimators equipped with a first order regularization seem to smooth the higher value of the curl and the div, yielding to high errors. Conversely, estimators with a div–curl smoothing (**A4** and **A6**) give reliable results. The results on the important out-of-plane velocity in case #8 confirm that the proposed ICE is a correct choice.

On this eight synthetic examples, the proposed method gives better results. We now turn to comparisons on two different types of real image sequences and compare our method with a classic PIV system.

6 Results for the mixing layer

6.1 Instantaneous velocity field

Images of the same instantaneous vector field are shown in Figs. 2(top) and 3(top), for Optical flow and PIV approach, respectively. Only one vector out of 225 were represented for optical flow. Results exhibit the footprint of the primary structures of the mixing layer. Based on vector fields both approaches gave comparable information but with higher density for optical flow. Figures 2(bottom) and 3(bottom) show contours of constant spanwise vorticity ω_z^*. When compared with PIV results, optical-flow approach exhibited more localized information. Nevertheless, vorticity yielded more noisy contours and higher levels of vorticity. As mentioned in Sect. 6.1, it might be possible that this noisy vorticity was due to the measurement noise in the input images.

6.2 Mean quantities

In a mixing layer, the mean streamwise velocity component can be expressed with the theoretical solution as:

$$\frac{\bar{U}-U_b}{U_a-U_b}=\frac{1}{2}(1-\mathrm{erf}(\sigma\eta)), \tag{18}$$

where $\eta=(y-y_o)/(x-x_o)$ with (x_o,y_o) the coordinate of the virtual origin of the mixing layer and where the spreading parameter σ is constant.

For each streamwise location x and for both approaches the experimental values fitted the theoretical solution. Results gathered in Table 2 show that the spreading parameter σ adjusted from optical flow and PIV II treatment was of the order of 49.8 and 43.6, respectively. Optical-flow value compared well with the value of 52.7 obtain by Heitz (1999) with pitot tube measurements, while PIV II gave poor agreement. For both approaches, the evolution of the vorticity thickness δ_ω, defined as $\delta_\omega=-\Delta U/(\partial U/\partial y)_{\max}$ where $\Delta U=U_a-U_b$, supported the observation of a linear growth of the

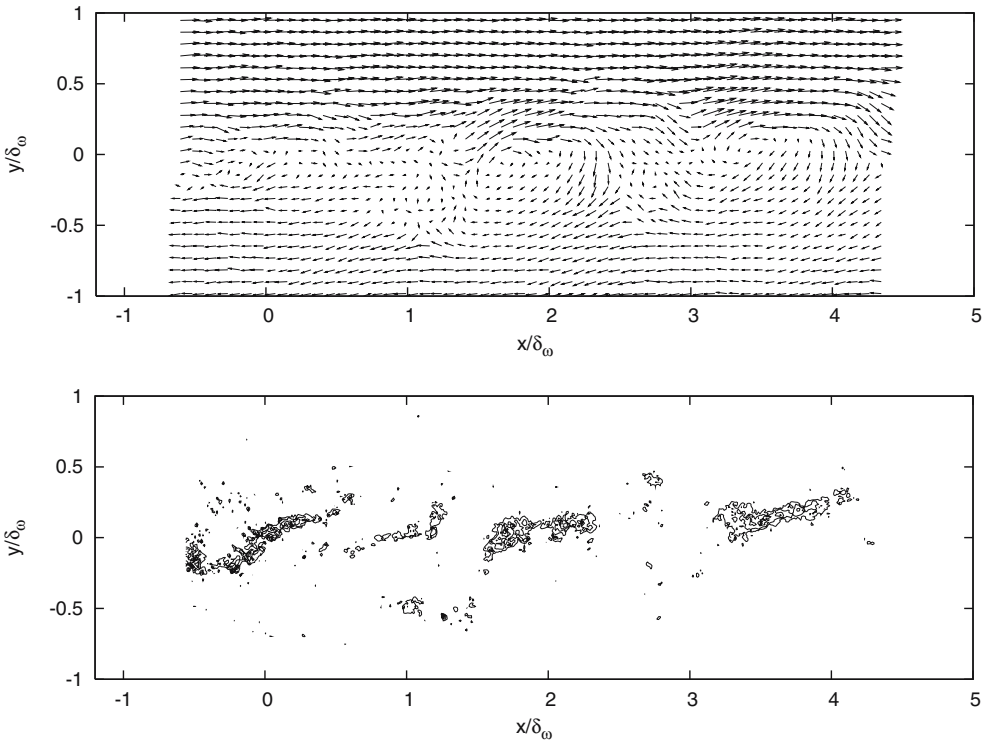

Fig. 2 Views of instantaneous turbulent plane mixing layer structure at $Re_{\delta_\omega} = 7,000$. Optical flow: *top*, instantaneous vector field (one vector out of 225); *bottom*, instantaneous spanwise isocontour of vorticity $\omega_z^* = (\omega_z \Delta U)/\delta_\omega (\omega^*_{z_{min}} = -9, \omega^*_{z_{max}} = -2, \Delta\omega_z^* = 1)$

mixing layer. As for the spreading parameter, PIV II results exhibited a higher growth of the mixing layer. This behaviour can be explained by the interrogation interval in which the velocity estimated was an average value, in a region where there were high displacements gradients.

To have a finer analysis, it is of primary interest to observe the superior order moments. To that end, the distribution of the Reynolds stress are represented in Fig. 4. Data were compared with (Heitz 1999) fourth hot-wire measurements. Results show that PIV I approach overestimated $\overline{u'^2}$ and underestimated $\overline{v'^2}$ and $\overline{u'v'}$. PIV II

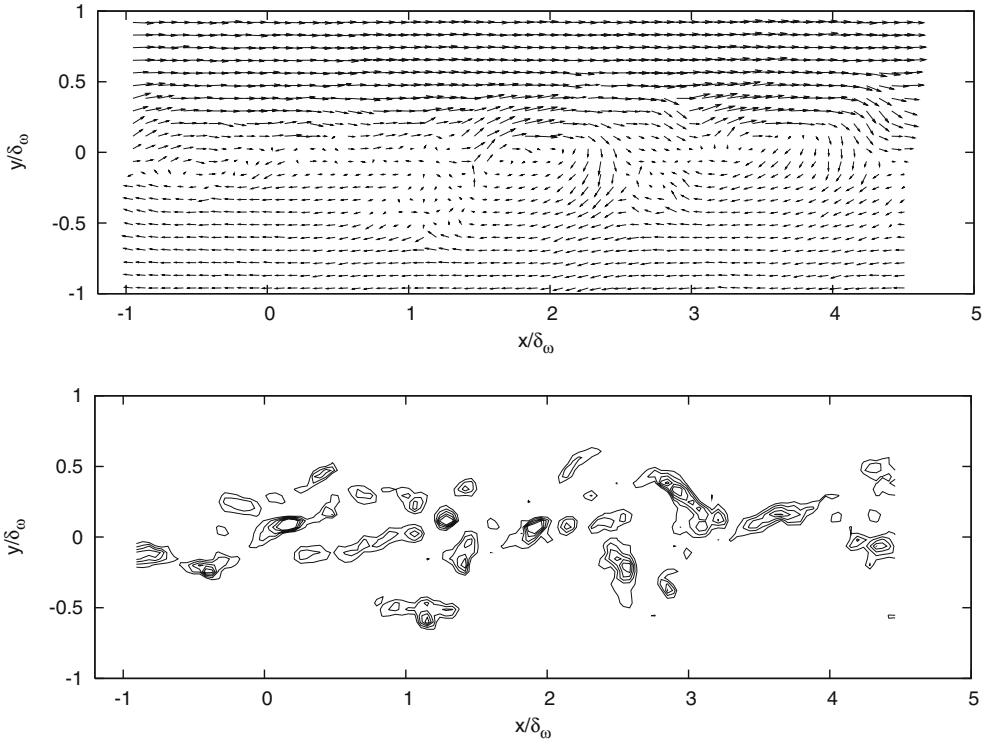

Fig. 3 Views of instantaneous turbulent plane mixing layer structure at $Re_{\delta_\omega} = 7,000$. PIV II—multipass 32-16 treatment: *top*, instantaneous vector field (one vector out of nine); *bottom*, instantaneous spanwise isocontour of vorticity $\omega_z^* = (\omega_z \Delta U)/\delta_\omega (\omega^*_{z_{min}} = -9, \omega^*_{z_{max}} = -2, \Delta\omega_z^* = 1)$

Table 2 Comparison on main characteristics parameters of the mixing layer for Pitot-tube measurements (Heitz 1999), PIV II and optical-flow approaches

	(Heitz 1999)	PIV	Optical flow
r	0.67	0.67	0.67
λ	0.2	0.2	0.2
σ	52.7	43.55	46.37
$d\delta_w/dx$	0.0336	0.0407	0.0382

approach gave better results with a slight overestimation of $\overline{u'^2}$ and $\overline{u'v'}$ and a slight underestimation of $\overline{v'^2}$. Optical-flow approach better fitted hot-wire measurements.

It should be noted that for PIV and optical-flow approaches the second order moments were computed with 520 samples, hence the Reynolds stress were not statistically converged values, whereas for hot-wire measurements more than 1,00,000 samples were collected. Nevertheless, we can say that both PIV and optical-flow approaches gave similar results in good agreement with the literature.

6.3 Discussions of results

This first experience proved the ability of the method presented in this article to recover dense motion fields from PIV images. Main characteristics of the flow (mixing layer mean characteristics and second-order moments) were recovered in a similar way with both approaches (PIV and the proposed optical-flow). A major difference between the two approaches was the number of vectors that the optical-flow technique was able to extract. Furthermore, it should be noted that optical-flow approach was able to extract more information (e.g. noisy) contained in the image than PIV approach did. Let us nevertheless remark that, from a time computation point of view, the presented method took nearly 120 s for estimation of an instantaneous dense motion field on a PC-linux (2.8 GHz, 1.5 Go-RAM) whereas the estimation with the PIV approach based on cross-correlation took only 15 s. If one is now interested in a pixel, the computation time is then of 121 μs/pix for the proposed approach whereas it is of 366 μs/pix for the correlation approach. In our experiments, we observed that the computation time for a pixel (at different image sizes) is slightly constant for the presented estimator. Some interrogations came also about the level of the noise obtained in the vorticity fields from the optical-flow method.

7 Results in the near wake of a circular cylinder

7.1 Instantaneous velocity field

Instantaneous velocity field and vorticity contours are shown in Figs. 5 and 6 for the proposed optical-flow approach and for the PIV approach, respectively.

The motion fields obtained from the two methods were very similar and correctly represented the physical phenomenon. Indeed, the main vortex launched in the middle of the image appears clearly in the velocity field as well as in iso-vorticity contours. In Figs. 5 and 6, these contours are very interesting to analyse. Indeed, it can be observed that both shared the main phenomena but that the major difference appeared in the spatial resolution, that of the optical-flow approach being highly superior. This led to a better topological description of the near wake flow. Nevertheless, a more

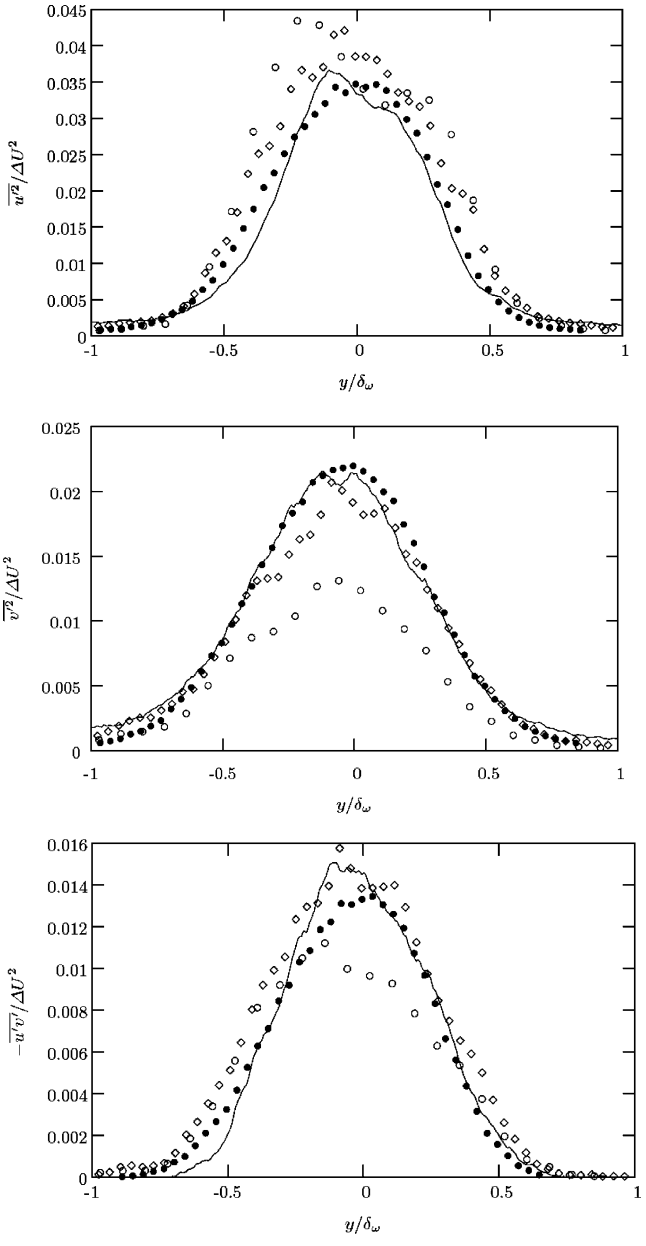

Fig. 4 Reynolds stress distributions of the mixing layer at $x/\delta_\omega = 4$. Each *symbol* representing a velocity measurement technique: *continuous line*, Optical flow; *open diamond*, PIV II; *open circle*, PIV I; *filled circle*, Hot wire (Heitz 1999)

precise study on this over-information must be carried out to reach its relevance. A work on that subject is currently in progress. Let us notice, as we previously mentioned, that the higher quality of the input images used for this experiment (a 12 bit CCD Pelletier cooled camera vs an 8 bit one for the mixing layer) was probably responsible of the better results, in terms of noise, of the vorticity map issued form the optical-flow velocity field.

7.2 Mean quantities

In this section, all motion fields from the 540 pairs of images of the whole sequence were computed. For both methods, mean velocity fields and their corresponding streamlines are represented in Fig. 7a, b, respectively.

At values of x/D greater than 1.5, the patterns of isocontours of the mean streamwise velocity remained roughly the same. At smaller values of x/D, the velocity pattern exhibits; however, slight differences in the description of the shear layers. Indeed, the same isovalue of the mean streamwise velocity, indicated a greater thickness of the shear layers with the optical-flow approach than with PIV. From the patterns of isocontours of the transverse mean velocity, represented in Fig. 7a, b, it appeared that results obtained with optical-flow approach were smoother than with PIV. This indicated that with the same number of samples, or data images, the statistical quantities exhibited more converged values with optical-flow than with PIV. In Fig. 8, this behaviour was readily observed with second-order moments, which converge later than first-order moments. Furthermore, these smoother results were associated with a better symmetry across the wake centreline. These differences can be explained by the global regularization methods, which is involved in the proposed algorithm and leads to homogeneous results, compared to PIV which is a local approach giving a mean value to each considered area.

The better representation of the patterns of the mean quantities gives a better location of the different maxima of u'^2 and v'^2 which are characteristics of the vortex formation region. Two main approaches can be distinguished to extract the streamwise length of the recirculation region: the distance between the base of the cylinder and the point with null longitudinal mean velocity ($U=0$) on the centreline of the flow ($y=0$), called the bubble length (L_R), and the distance to the point where the $(u'^2+v'^2)$ quantity is maximum on the centreline, called the formation length (L_f). The latter criterion defined by Bloor and Gerrard (1966) enables to compare results with single hot-wire cooling velocity measurements. Single hot-wire measurements were carried out with the wire parallel to the axis of the cylinder $y-$axis, so that measurements were more sensitive to the cross-flow induced by the formation of the Kármán

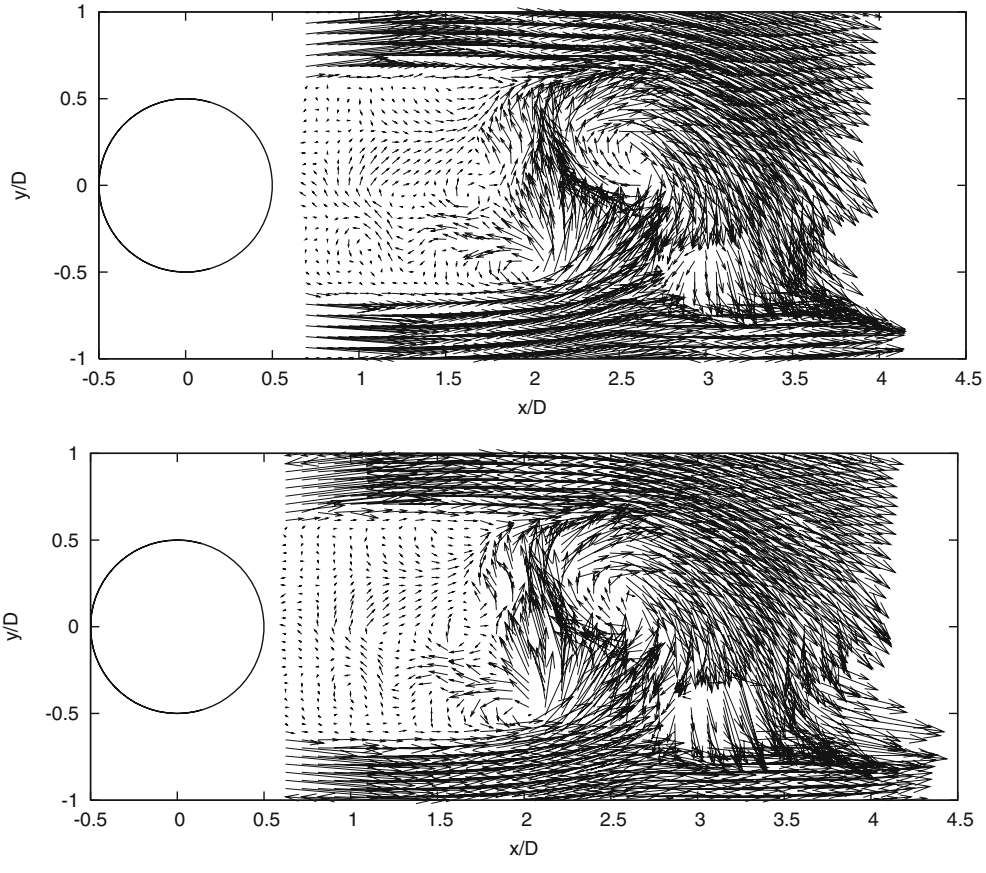

Fig. 5 View of instantaneous near wake vector field at $Re=3{,}000$: *top*, optical-flow treatment (one vector out of 256); *bottom*, PIV treatment (one vector out of four)

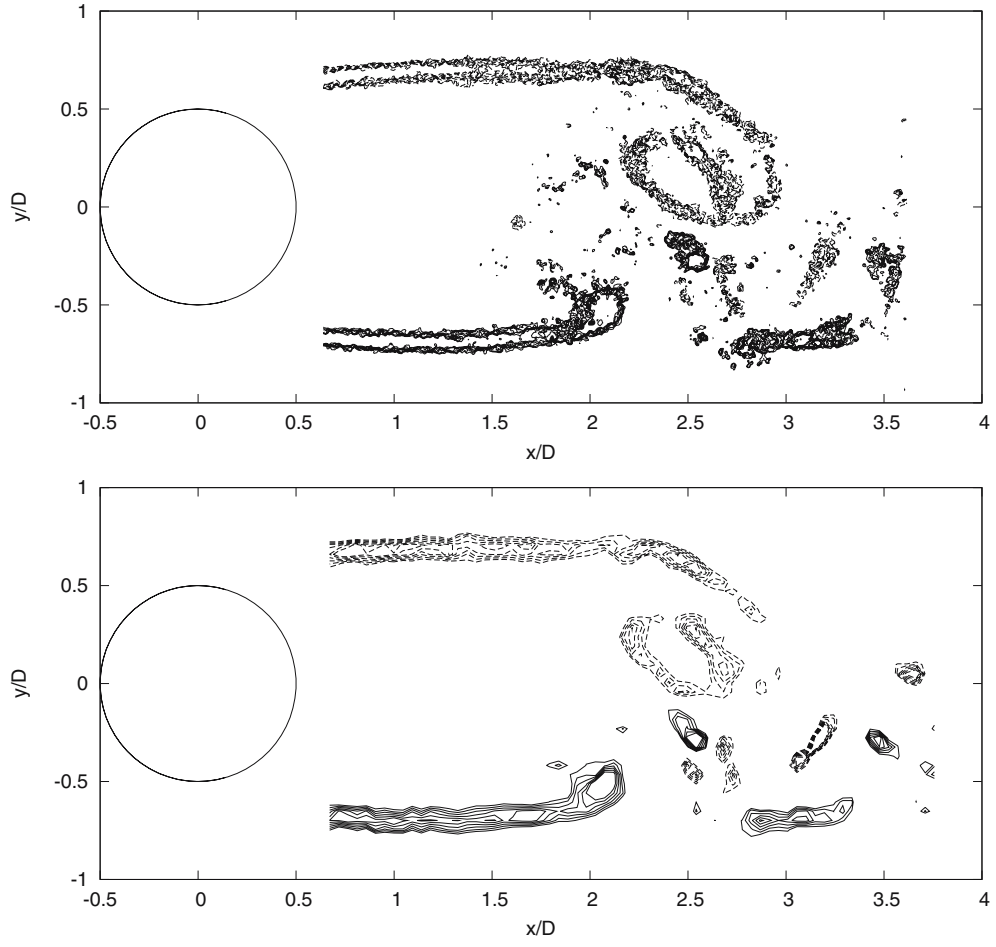

Fig. 6 View of instantaneous near wake iso-contour of vorticity at $Re = 3,000 - \omega_z^* = (\omega_z U)/D$ ($|\omega_{z_{\min}}^*| = 0.5, |\omega_{z_{\max}}^*| = 10$, $\Delta\omega_z^* = 1$) : *top*, optical-flow treatment; *bottom*, PIV treatment

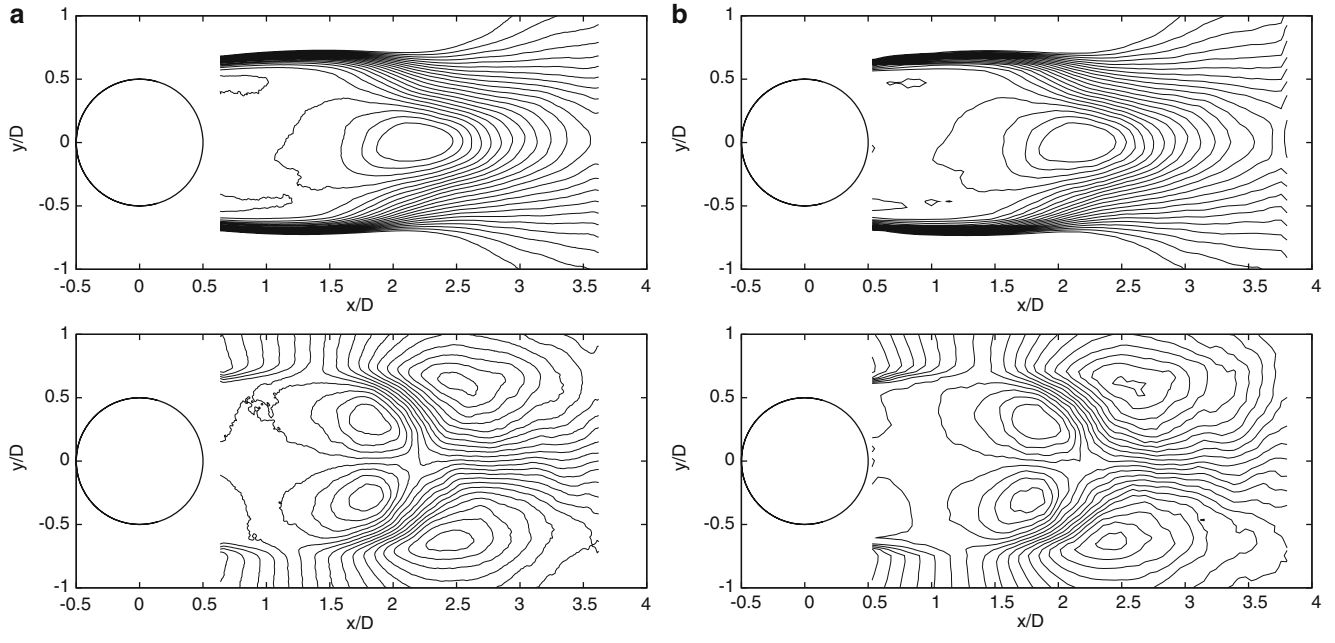

Fig. 7 From *top* to *bottom*, 21 iso-contours of mean streamwise velocity $U/U_\infty = -0.2,...,1$ and of mean transverse velocity $V/U_\infty = -0.25,...,0.25$: **a**, optical-flow measurements; **b**, PIV measurements

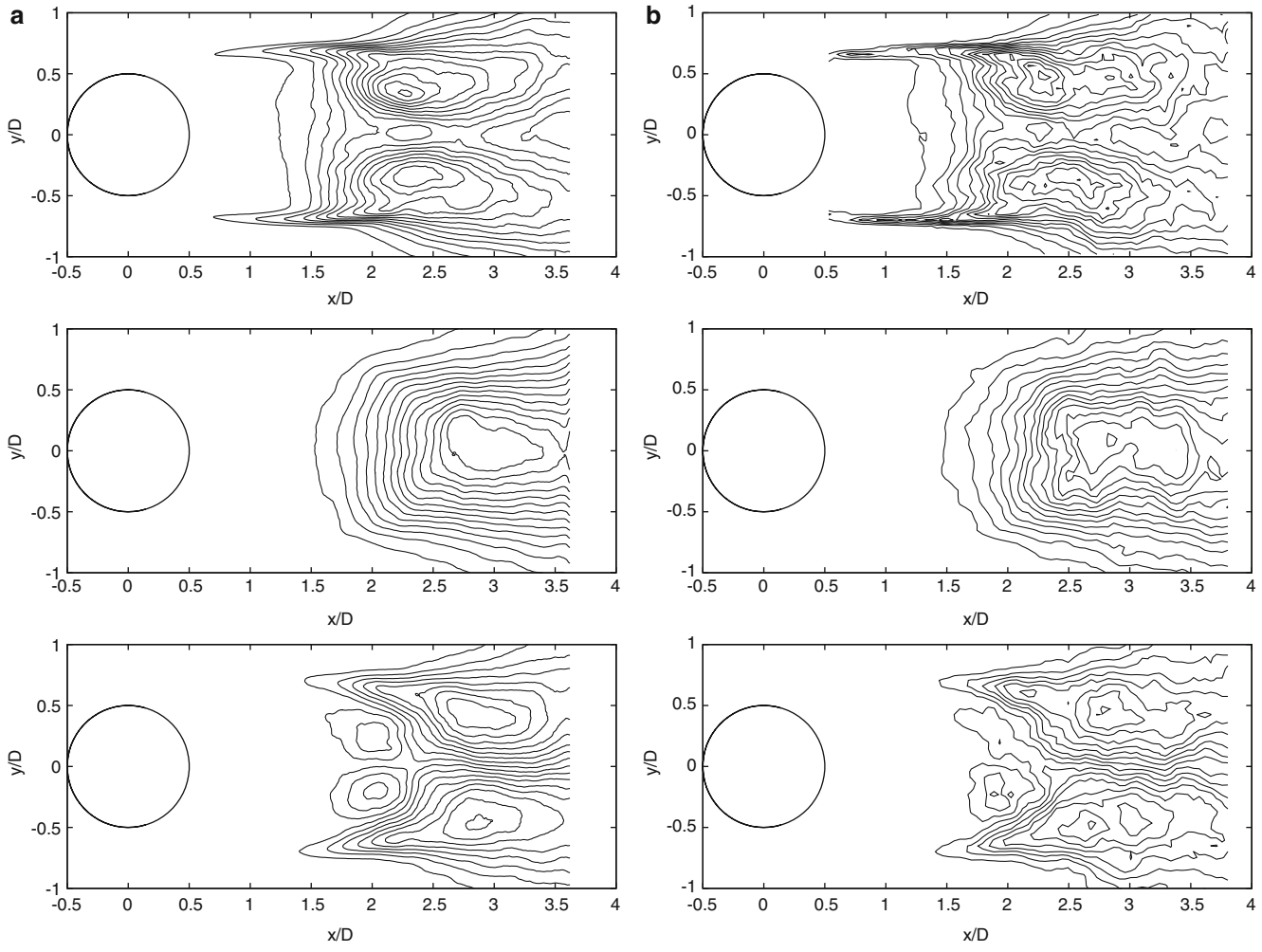

Fig. 8 From *top* to *bottom*, 15 iso-contours of $\overline{u'^2}/U_\infty^2 = 0, \ldots, 0.05$, $\overline{v'^2}/U_\infty^2 = 0, \ldots, 0.1$ and $\overline{u'v'}/U_\infty^2 = -0.025, \ldots, 0.025$: **a** optical-flow measurements; **b** PIV measurements

vortices. Critical values along the wake centreline are presented in Table 3. Results show that the bubble length was nearly the same for optical-flow and PIV methods, whereas the formation length was better determined with the former approach, close to hot-wire measurements, than with the latter one. Presumably, this may be related to the better extraction, with optical-flow schemes, of the vortices formed and launched in the very near wake, as it is shown in Fig. 6. It should be noticed that, due to the low aspect ratio ($L/D = 14.2$ without end plates), the critical values along the wake centreline yielded larger mean longitudinal velocity minimum and formation length than those observed when the aspect ratio was sufficiently large to be independent of this parameter.

Table 3 Critical values along the wake centreline, $y = 0$

	Hot wire	PIV	Optical flow
$U_{\min}/U_\infty$	–	−0.30	−0.29
L_R/D	–	2.70	2.73
L_f/D	2.80	2.71	2.85

To have a quantitative idea of the relevance of different results, we represent in Figs. 9 and 10 mean velocity and Reynolds stress profiles at two locations downstream of the cylinder ($x/D = 1.56$ and $x/D = 3.6$). For both algorithms, mean velocity distributions were in good agreement. Concerning Reynolds stress, the shape of all curves were quite similar. However, their local extrema were different. For $x/D = 1.56$, optical-flow underestimated the fluctuating velocity levels compared to PIV. Let us recall that this region corresponds to the free shear layers spreading, which for the subcritical regime concerned, exhibits small vorticity thicknesses with large gradients. The proposed algorithm, which is based on a global regularization, uses a quadratic smoothness constraint $\mathscr{H}_{\text{reg}}$ which enforces a spatial smoothness of the divergence and the vorticity of the motion field. This may explain the lower value of each extremum provided by the optical-flow estimator.

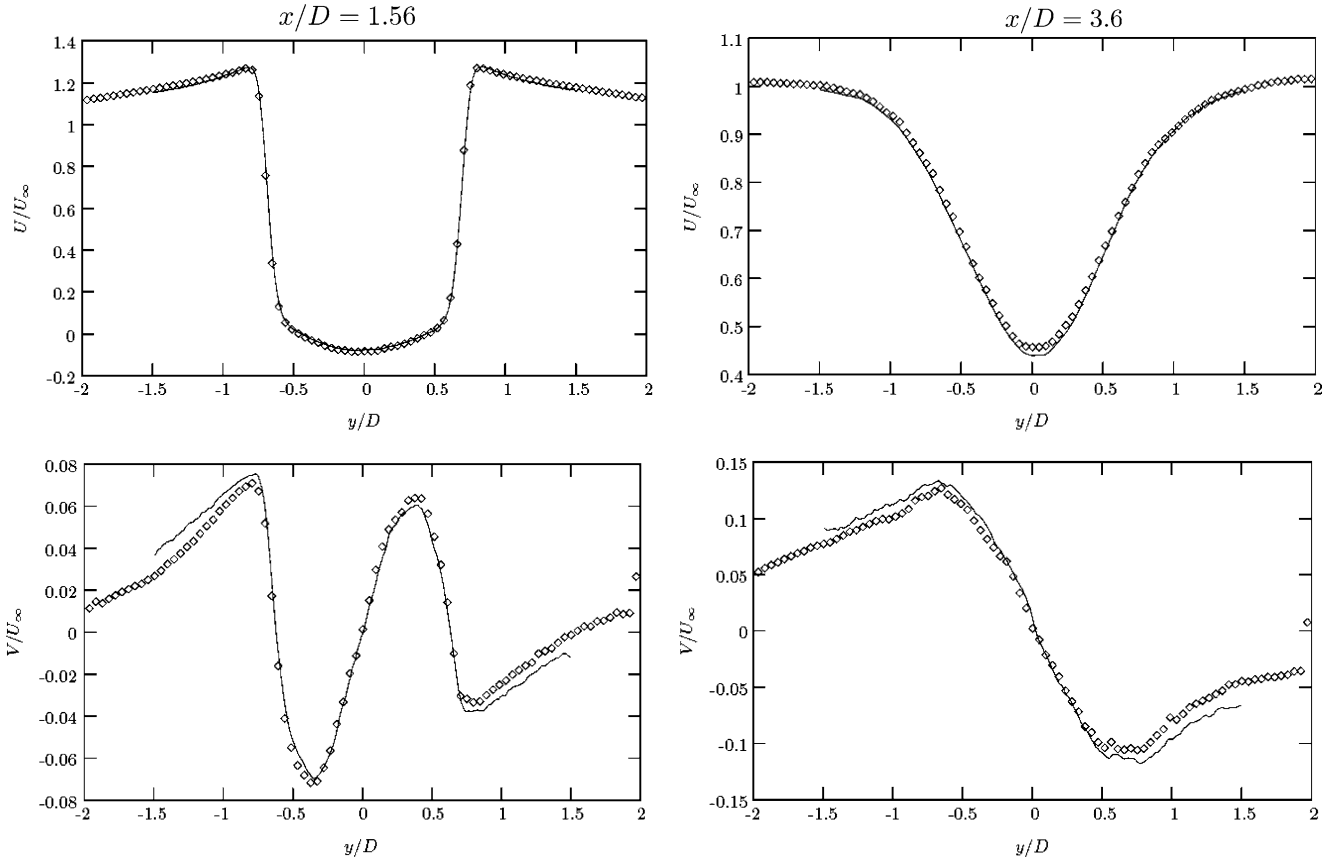

Fig. 9 Comparison of profiles of mean velocity components U and V at two locations downstream of the cylinder: *continuous line*, optical-flow measurements; *open diamond*, PIV measurements

Further improvements could be obtained using a robust penalty function f_2 is the second part of the regularization term of Eq. 15:

$$\alpha \iint_{\Omega} |\mathrm{div}\boldsymbol{d} - \xi|^2 + \lambda f_2(\|\nabla\xi\|) + \alpha \iint_{\Omega} |\mathrm{curl}\boldsymbol{d} - \zeta|^2 + \lambda f_2(\|\nabla\zeta\|)$$

Such a penalty term should be able to obtain better estimates of the motion fields and in particular to extract better local extrema of the Reynolds stress. Nevertheless, this form yields to the definition of an other threshold parameter. In order to quantify the effect of a robust penalty function, new research studies with dedicated experiments are currently in progress in our laboratories. For $x/D = 3.6$, the differences between the two approaches were consistent with the distinct estimation of the recirculation region, seen above for the formation length.

8 Conclusion

In this paper, we have experimentally evaluated a new method for estimating instantaneous velocities of fluid flows from image sequences. This method is an extension of the standard optical-flow based approaches used in computer vision where a robust objective function is minimized. The two parts (i.e, the data term and the regularizer) of the novel cost function have been specifically designed to suit image sequences of fluid flows.

The data term is based on a continuity equation, as a more physically-grounded alternative to the usual brightness constancy assumption. To be compatible with large displacements, we chose to use it in an integrated form. Such situations occur when the imaged flow is fast (like in most of the fluid experiments), or when the temporal sampling rate is low (as with satellite images).

As for the regularization, we state that only a second-order regularizer is able to preserve completely the divergence and vorticity structures of the flows. Using the div–curl formalism, we thus introduced a second-order regularizer which captures the divergence and vorticity of the unknown flow.

The developed approach has been tested on synthetic images (issued from the VSJ) and on two experimental flows representing a mixing layer and the near wake of a circular cylinder, respectively. In each case, we compared our results with the ones issued from PIV. It can be pointed out that main parameters values extracted with both methods had the same order of magnitude. The relevance of the obtained motion fields was then

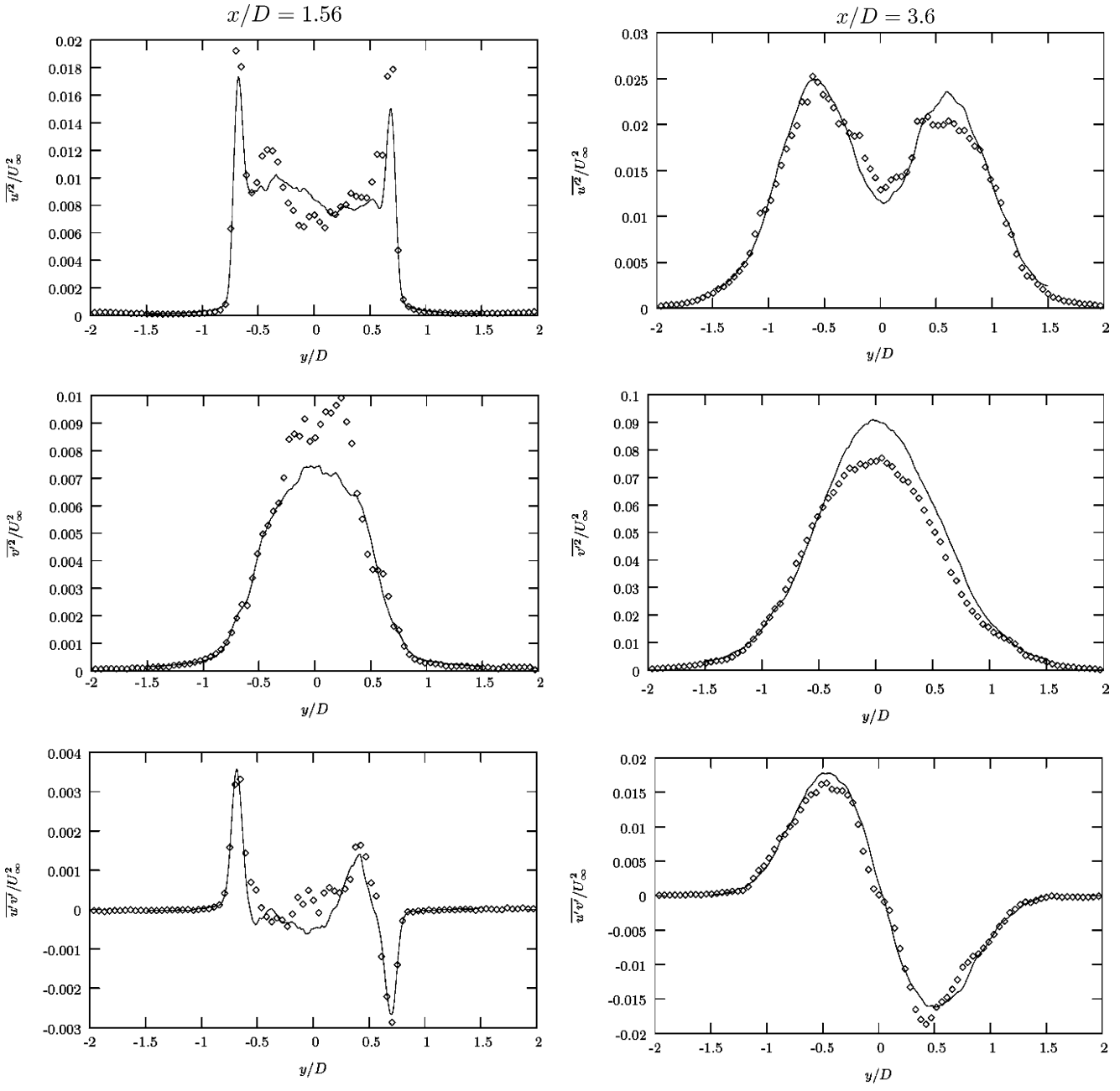

Fig. 10 Comparison of profiles of Reynolds stresses at two locations downstream of a cylinder: *continuous line*, optical-flow measurements; *open diamond*, PIV measurements

similar. A major difference comes from the number of vectors that the presented technique is able to estimate. Let us recall that a *dense* motion field was obtained (i.e. one vector per pixel). In a future work, new tests will be carried out to optimize the accuracy of the dense information given by the optical flow method.

Acknowledgements The authors would like to thank Joel Delville (University of Poitiers, France) and Beatriz Camano (Rio Grande do Sul Federal University, Brazil) for their valuable contribution on mixing layer experiments. The financial support by the Region Bretagne of France under grant no. 20048347, by the French Ministry of Research under grant no. 032593, and by the European Union under grant no. FP6-513663 are gratefully acknowledged.

9 Appendix A: Div–Curl versus first-order regularization

By using the *Euler–Lagrange* condition of minimality, the equivalence between a standard first-order smoothness regularization, and a div–curl regularization with same weights for div and curl penalties can be readily demonstrated. Recall that Euler–Lagrange equation

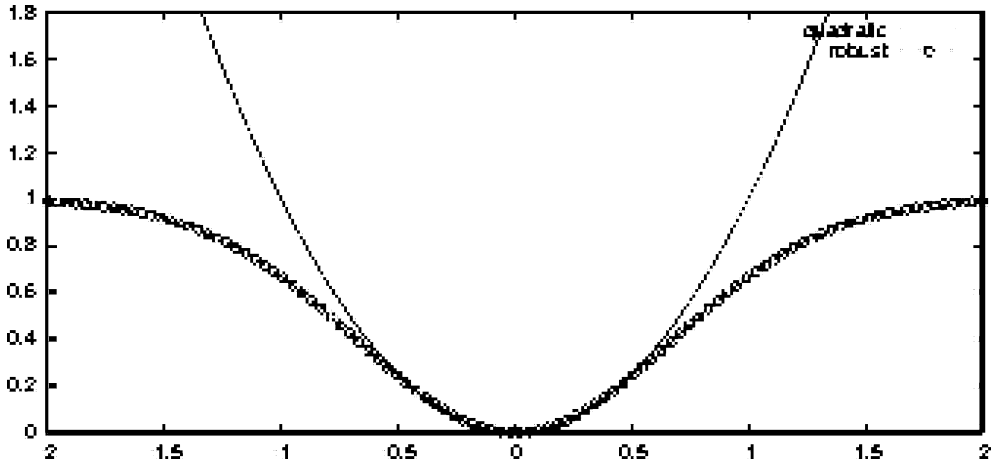

Fig. 11 Comparison of the shape of the Leclerc robust penalization (*bottom*) (with $\tau_1 = 1$) versus the quadratic one (*top*)

constitutes a necessary conditions for the minimization with respect to function $g(x,y)$ of a functional

$$\int_{\Omega} \mathscr{F}(g, g_x, g_y, x, y)\mathrm{d}\boldsymbol{x}.$$

It reads,

$$\frac{\partial \mathscr{F}}{\partial g} - \frac{\partial}{\partial x}\frac{\partial \mathscr{F}}{\partial g_x} - \frac{\partial}{\partial y}\frac{\partial \mathscr{F}}{\partial g_y} = 0$$

Assuming a first-order regularization term

$$\mathscr{H}_{\mathrm{reg}}(\boldsymbol{d}) = \alpha \int_{\Omega} (|\nabla u(\boldsymbol{x})|^2 + |\nabla v(\boldsymbol{x})|^2)\mathrm{d}\boldsymbol{x},$$

this condition amounts to the following coupled PDEs:

$$\begin{cases} -2\alpha u_{xx} - 2\alpha u_{yy} = 0 \\ -2\alpha v_{xx} - 2\alpha v_{yy} = 0. \end{cases} \tag{19}$$

Now, considering a div–curl regularization

$$\mathscr{H}_{\mathrm{reg}}(\boldsymbol{d}) = \int_{\Omega} \left(\alpha \mathrm{div}^2 \boldsymbol{d}(\boldsymbol{x}) + \beta \mathrm{curl}^2 \boldsymbol{d}(\boldsymbol{x})\right)\mathrm{d}\boldsymbol{x}, \tag{20}$$

the Euler–Lagrange equations reads,

$$\begin{cases} -2\alpha u_{xx} - 2\beta u_{yy} - 2(\alpha - \beta) v_{xy} = 0 \\ -2\beta v_{xx} - 2\alpha v_{yy} - 2(\alpha - \beta) v_{xy} = 0. \end{cases} \tag{21}$$

When $\alpha = \beta$, these equations are the same as Eq. 19

10 Appendix B: Robust penalization

The main objective of robust estimators is to impose a different penalization for coherent and incoherent data: when the error to minimize is small (e.g. data are in accordance with underlying assumptions), the robust function tends to the L_2 quadratic norm; when this error is high (*e.g.* presence of outliers), it tends to attenuate the contribution of the error term (and then to be softer than the quadratic function). Figure 11 presents a possible shape of such function (the Leclerc penalty function: $f_1(x) = 1 - \exp(-\tau_1\ x^2)$).

The choice of robust penalty functions needs to define the parameter τ_1 and generally makes the problem non-quadratic. The specific minimization problem we face is classically turned into an augmented half-quadratic minimization problem (Holland and Welsch 1977). Indeed, with all robust penalty functions f such that $f(\sqrt{.})$ is concave (as the Leclerc one), we have the property that:

$$f(x) = \min_{z \in (m,M]} zx^2 + \psi(z), \tag{22}$$

where $M = \lim_{0^+} \frac{f'(x)}{2x}$, $m = \lim_{+\infty} \frac{f'(x)}{2x}$, and ψ, for which an expression can be found in (Black and Rangarajan 1996; Geman and Reynolds 1992), is such that the minimizer on the right-hand-side is given by $z = \frac{f'(x)}{2x}$.

Using Eq. 22, each minimization problem of the generic form $\min_x \sum_k f(g_k(x))$ can be replaced by the auxiliary problem $\min_{x,\{z_k\}} \sum_k z_k g_k^2(x) + \psi(z_k)$, which can be solved by iteratively re-weighted least squares (IRLS) (Holland and Welsch 1977): for fixed auxiliary (weight) variables $z_k \in (m,M]$, one faces a least-squares problem; for fixed x, the optimal value for each weight is known in closed form as $\frac{f'(g_k(x))}{2g_k(x)}$. This process is done until convergence.

References

Adrian R (1991) Particle imaging techniques for experimental fluid mechanics. Annal Rev Fluid Mech 23:261–304

Amini A (1994) A scalar function formulation for optical flow. In: Proceedings Europ Conf Computer Vision, pp 125–131

Bannehr L, Rohn R, Warnecke G (1996) A functional analytic method to derive displacement vector fields from satellite image sequences. Int J Remote Sensing 17(2):383–392

Barron J, Fleet D, Beauchemin S (1994) Performance of optical flow techniques. Int J Comput Vision 12(1):43–77

Béréziat D, Herlin I, Younes L (2000) A generalized optical flow constraint and its physical interpretation. In: Proceedings Conf Comp Vision Pattern Rec, vol 2, pp 487–492, Hilton Head Island, South Carolina, USA, 2000

Black M (1994) Recursive non-linear estimation of discontinuous flow fields. In: Proceedings Europ Conf Computer Vision, pp 138–145, Stockholm, Sweden, 1994

Black M, Rangarajan A (1996) On the unification of line processes, outlier rejection, and robust statistics with applications in early vision. Int J Comput Vision 19(1):75–104

Bloor MS, Gerrard JH (1966) Measurements on turbulent vortices in a cylinder wake. Proc R Soc Lond 294:319–342

Cohen I, Herlin I (1999) Non uniform multiresolution method for optical flow and phase portrait models: environmental applications. Int J Comput Vision 33(1):29–49

Corpetti T, Mémin E, Pérez P (2002) Dense estimation of fluid flows. IEEE Trans Pattern Anal Mach Intell 24(3):365–380

Fitzpatrick JM (1988) The existence of geometrical density-image transformations corresponding to object motion. Comput Vision Graph Image Proc 44(2):155–174

Geman D, Reynolds G (1992) Constrained restoration and the recovery of discontinuities. IEEE Trans Pattern Anal Mach Intell 14(3):367–383

Gupta S, Prince J (1996) Stochastic models for div-curl optical flow methods. Signal Proc Lett 3(2):32–34

Heitz D (1999) Etude expérimentale du sillage d'un barreau cylindrique se développant dans une couche de mélange plane turbulente. PhD thesis, Université de Poitiers, 1999

Holland P, Welsch R (1977) Robust regression using iteratively reweighted least-squares. Commun Statis Theor Meth A6(9):813–827

Horn B, Schunck B (1981) Determining optical flow. Artif Intell 17:185–203

Huber P (1981) Robust statistics. Wiley, New York

Kornprobst P, Deriche R, Aubert G (1999) Image sequence analysis via partial differential equations. J Math Imaging Vis 11(1):5–26

Larsen R, Conradsen K, Ersboll BK (1998) Estimation of dense image flow fields in fluids. IEEE Trans Geosci Remote sensing 36(1):256–264

Lecuona A, Ruiz-Rivas U, Rodriguez-Aumente P (2002) Near field vortex dynamics in axially forced, co-flowing jets: quantitative description of a low-frequency configuration. Euro J Mech B/Fluid 21:701–720

Lourenco L, Krothapalli A (1995) On the accuracy of velocity and vorticity measurements with piv. Exp Fluid 18:421–428

Lourenco L, Krothapalli A (2000) True resolution piv: a mesh-free second-order accurate algoritm. In: 10th International symposium on applications of laser techniques in fluid mechanics, Lisbon, Portugal, July 2000

McKenna SP, McGillis WR (2002) Performance of digital image velocimetry processing techniques. Exp Fluid 32:106–115

Mémin E, Pérez P (1998) Dense estimation and object-based segmentation of the optical flow with robust techniques. IEEE Trans Image Process 7(5):703–719

Mémin E, Pérez P (1998) A multigrid approach for hierarchical motion estimation. In: Proceedings of international conference on computer vision, pp 933–938, Bombay, India

Mémin E, Pérez P (1999) Fluid motion recovery by coupling dense and parametric motion fields. In: Proceedings of international conference on computer vision, vol 3, pp 732–736, Corfou, Greece

Mémin E, Pérez P (2002) Hierarchical estimation and segmentation of dense motion fields. Int J Comput Vision 46(2):129–155

Nogueira J, Lecuona A, Rodriguez PA (2001) Identification of a new source of peak locking, analysis and its removal in conventional and super-resolution PIV techniques. Exp Fluid 30:309–316

Nomura A, Miike H, Koga K (1991) Field theory approach for determining optical flow. Pattern Recogn Lett 12(3):183–190

Okamoto K, Nishio S, Saga T, Kobayashi T (2000) Standard images for PIV. MST 11, pp 685–691

Quénot GM (1999) Performance evaluation of an optical flow technique applied to PIV using the VSJ standard images. In: 3rd International workshop on PIV, pp 579–584

Quénot GM, Pakleza J, Kowalewski A (1998) Particle image velocimetry with optical flow. Exp Fluid 25(3):177–189

Raffel M, Willert C, Kompenhans J (2000) Particle image velocimetry. Springer, Berlin Heidelberg New York

Ruhnau P, Kohlberger T, Schnörr C, Nobach H (2005) Variational optical flow estimation for particle image velocimetry. Exp Fluids, pp 21–32

Scarano F, Reithmuller LM (2000) Advances in iterative multigrid piv image processing. Exp Fluids [Suppl]:S51–S60

Schunk BG (1984) The motion constraint equation for optical flow. In: Proceedings Int Conf Pattern Recognition, pp 20–22, Montreal

Song SM, Leahy RM (1991) Computation of 3D velocity fields from 3D cine and CT images of human heart. IEEE Trans Med Imaging 10(3):295–306

Suter D (1994) Motion estimation and vector splines. In: Proceedings Conf Comp Vision Pattern Rec, pp 939–942, Seattle, USA, June 1994

Wallace J, Foss J (1995) The measurement of vorticity in turbulent flows. Annu Rev Fluid Mech 27:469–514

Wereley ST, Meinhart CD (2001) Second-order accurate particule image velocimetry. Exp Fluid 31:258–268

Wernert P, Geissler W, Raffel M, Kompenhans J (1996) Experimental and numerical investigations of dynamic stall on a pitching airfoil. AIAA J 34(5):982–989

Wildes R, Amabile M, Lanzillotto AM, Leu TS (1997) Physically based fluid flow recovery from image sequences. In: Proceedings Conf Comp Vision Pattern Rec, pp 969–975

Willert CE, Gharib M (1991) Digital particle image velocimetry. Exp Fluid 10:181–193

Zhou L, Kambhamettu C, Goldgof D (2000) Fluid structure and motion analysis from multi-spectrum 2D cloud images sequences. In: Proceedings Conf Comp Vision Pattern Rec, vol 2, pp 744–751, Hilton Head Island, South Carolina, USA, 2000